ITERATIVE MULTISTAGE MODEL-BASED DECOMPOSITION FOR POLARIMETRIC SYNTHETIC APERTURE RADAR IMAGERY

Ken Yoong LEE, Chen Guang HOU, Soo Chin LIEW and Leong Keong KWOH

Centre for Remote Imaging, Sensing and Processing
National University of Singapore
10 Lower Kent Ridge Road, Block S17, Level 2, Singapore 119076
E-mail: {crslky, crshc, scliew, crsklk}@nus.edu.sg

KEY WORDS: Synthetic aperture radar, radar polarimetry, scattering mechanisms, model-based polarimetric decomposition, ALOS-2 PALSAR-2

ABSTRACT: This paper re-examines our previously proposed multistage four-component polarimetric decomposition for reducing negative power pixels, where the performance evaluation was conducted by using ALOS-2 PALSAR-2 fully polarimetric data. The negative power pixels over vegetated areas were significantly reduced. The remaining negative power pixels distributed primarily over man-made objects and sea. For further reduction, an iterative multistage polarimetric decomposition, which employs two roll-invariant volume scattering models, was subsequently developed. The derived physical scattering mechanisms of different land cover types were analysed and are reported in this paper.

1. INTRODUCTION

The retrieval of physical scattering properties of different land cover features from polarimetric synthetic aperture radar (PolSAR) data has long been studied since last three decades (van Zyl, 1989; Freeman and Durden, 1992; Cloude and Pottier, 1997). A three-component scattering model was developed by Freeman and Durden (1992, 1998) for multilook PolSAR data. Their model involves physical fitting of a combination of double-bounce, surface, and volume scattering mechanisms. Since then, the model-based polarimetric decomposition has received a considerable amount of attention in the literature (Yajima *et al*., 2008; Arii *et al*., 2011; Hong and Wdowinski, 2014; Singh and Yamaguchi, 2018). Yamaguchi *et al*. (2005) extended the Freeman-Durden model by adding helix scattering. One well-known problem associated with the model-based decomposition is the presence of negative scattering powers, which is inconsistent with the actual scattering phenomenon (Yamaguchi *et al*., 2005; van Zyl *et al*., 2008, 2011; An *et al*., 2010; Lee *et al*., 2014). Recently, we proposed a multistage four-component decomposition (Lee *et al*., 2018), which is inspired by the generalised odd-bounce and double-bounce scattering models (Chen *et al*., 2014), for reducing negative power pixels. Its performance was evaluated by using NASA/JPL AIRSAR PolSAR C- and L-band data. The experimental results showed that a large amount of negative power pixels over vegetated areas, such as grassland and tree cover, were reduced.

In this paper an extended work is carried out to examine our previously proposed multistage model-based decomposition by using ALOS-2 PALSAR-2 fully polarimetric data. Sections 2 and 3 present separately the Yamaguchi's and multistage four-component polarimetric decompositions. The details of the ALOS-2 PALSAR-2 test data are described in Section 4. Section 5 discusses the experimental decomposition and scattering classification results. Finally, the conclusions are given in Section 6.

2. YAMAGUCHI'S FOUR-COMPONENT POLARIMETRIC DECOMPOSITION

Freeman and Durden (1992, 1998) introduced a model-fitting approach for retrieving three elementary scattering mechanisms, namely, surface scattering, double-bounce scattering, and volume scattering, from the polarimetric covariance matrix of each pixel in multilook PolSAR data. The three-component scattering model was extended by Yamaguchi *et al*. (2005) by adding helix scattering. In a further work, Yamaguchi *et al*. (2006) reformulated their four-component decomposition through the coherency matrix representation.

For the surface scattering, the first-order Bragg model is used for a moderately rough surface. Its scattering vector in the Pauli basis is given by

$$\mathbf{k}_s = \begin{bmatrix} B_{HH} + B_{VV} \\ B_{HH} - B_{VV} \\ 0 \end{bmatrix}. \tag{1}$$

The complex values B_{HH} and B_{VV} are separately the reflection coefficients of HH and VV polarisations (Cloude and Pottier, 1996):

$$B_{HH} = \frac{\cos\phi - \sqrt{\varepsilon_r - \sin^2\phi}}{\cos\phi + \sqrt{\varepsilon_r - \sin^2\phi}}, \tag{2}$$

$$B_{VV} = \frac{(\varepsilon_r - 1)\{\sin^2\phi - \varepsilon_r (1 + \sin^2\phi)\}}{\left(\varepsilon_r \cos\phi + \sqrt{\varepsilon_r - \sin^2\phi}\right)^2}, \tag{3}$$

where ϕ is the local incidence angle and ε_r is the relative dielectric constant of the surface. The coherency matrix of a surface scattering response can then be obtained as follows:

$$\mathbf{T}_s = \mathbf{k}_s \mathbf{k}_s^{*T} = \begin{bmatrix} 1 & \beta^* & 0 \\ \beta & |\beta|^2 & 0 \\ 0 & 0 & 0 \end{bmatrix}, \tag{4}$$

where $\beta = (B_{HH} - B_{VV}) / (B_{HH} + B_{VV})$ and $|\beta| < 1$. The superscripts $*$ and T denote separately the complex conjugate and transpose. $|.|$ represents the absolute value.

The double-bounce scattering component is modelled by scattering from a dihedral corner reflector, where two orthogonal surfaces can be made of different dielectric materials. Its Pauli scattering vector is

$$\mathbf{k}_d = \begin{bmatrix} R_{H1}R_{H2} - R_{V1}R_{V2} \\ R_{H1}R_{H2} + R_{V1}R_{V2} \\ 0 \end{bmatrix}, \tag{5}$$

where $j = \sqrt{-1}$. The R terms represent the Fresnel reflection coefficients of the first and second surfaces. Thus, the coherency matrix of a double-bounce scattering is given by

$$\mathbf{T}_d = \mathbf{k}_d \mathbf{k}_d^{*T} = \begin{bmatrix} |\alpha|^2 & \alpha & 0 \\ \alpha^* & 1 & 0 \\ 0 & 0 & 0 \end{bmatrix}, \tag{6}$$

where

$$\alpha = \frac{R_{H1}R_{H2} - R_{V1}R_{V2}}{R_{H1}R_{H2} + R_{V1}R_{V2}} \tag{7}$$

and $|\alpha| < 1$.

For the volume scattering, the radar returns are assumed from a cloud of randomly oriented, very thin, cylinder-like dipoles. By further assuming a uniform distribution for the orientation angle of the dipoles, the corresponding coherency matrix is expressed in Yamaguchi *et al*. (2006, p. 293) as

$$\mathbf{T}_v = \frac{1}{4}\begin{bmatrix} 2 & 0 & 0 \\ 0 & 1 & 0 \\ 0 & 0 & 1 \end{bmatrix}. \tag{8}$$

For the roll-invariant helix scattering, its coherency matrix is of the form

$$\mathbf{T}_h = \frac{1}{2}\begin{bmatrix} 0 & 0 & 0 \\ 0 & 1 & \pm j \\ 0 & \mp j & 1 \end{bmatrix}. \tag{9}$$

By assuming that all the four scattering mechanisms are uncorrelated, the four-component decomposition for the coherency matrix of a pixel in multilook PolSAR data is given by

$$\mathbf{T} = f_s\mathbf{T}_s + f_d\mathbf{T}_d + f_v\mathbf{T}_v + f_h\mathbf{T}_h. \tag{10}$$

From (10), six equations with eight unknowns are found:

$$t_{11} = f_s + f_d \mid \alpha \mid^2 + f_v/2, \tag{11}$$
$$t_{22} = f_s \mid \beta \mid^2 + f_d + f_v/4 + f_h/2, \tag{12}$$
$$t_{33} = f_v/4 + f_h/2, \tag{13}$$
$$\Re(t_{12}) = f_s\Re(\beta^*) + f_d\Re(\alpha), \tag{14}$$
$$\Im(t_{12}) = f_s\Im(\beta^*) + f_d\Im(\alpha), \tag{15}$$
$$\Im(t_{23}) = \pm f_h/2, \tag{16}$$

where f_s, f_d, f_v, and f_h are the real coefficients corresponding to the surface, double-bounce, volume, and helix scattering contributions. $\Re(.)$ and $\Im(.)$ represent the real and imaginary parts, respectively. In order to solve (10), α is set to zero if $\langle\Re(s_{HH}s_{VV}^*)\rangle$ is positive, which implies that the surface scatter is dominant. Note that $s_{HH}s_{VV}^*$ refers to the Hermitian product of HH and VV polarisations. If $\langle\Re(s_{HH}s_{VV}^*)\rangle$ is negative, the double-bounce scatter is dominant and β is subsequently fixed to zero.

With the obtained f_s, f_d, f_v, f_h, α, and β, the contribution of each scattering mechanism to the total power P can be estimated as

$$P = P_s + P_d + P_v + P_h, \tag{17}$$

where

$$P_s = f_s\,(1 + |\beta|^2), \tag{18}$$
$$P_d = f_d\,(1 + |\alpha|^2), \tag{19}$$
$$P_v = f_v, \tag{20}$$
$$P_h = f_h. \tag{21}$$

The powers P_s, P_d, P_v, and P_h denote the contributions of the surface scattering, double-bounce scattering, volume scattering, and helix scattering in each pixel of PolSAR data.

3. MULTISTAGE FOUR-COMPONENT POLARIMETRIC DECOMPOSITION

Chen *et al*. (2014, p. 1845) generalised the odd-bounce and double-bounce scattering models by considering the rotation angle θ about the radar line of sight. The coherency matrix for the generalised odd-bounce model takes the form

$$\mathbf{T}_s(\theta_s) = \mathbf{R}\mathbf{T}_s\mathbf{R}^T = \begin{bmatrix} 1 & \beta^* \cos 2\theta_s & -\beta^* \sin 2\theta_s \\ \beta \cos 2\theta_s & |\beta|^2 \cos^2 2\theta_s & -\frac{1}{2}|\beta|^2 \sin 4\theta_s \\ -\beta \sin 2\theta_s & -\frac{1}{2}|\beta|^2 \sin 4\theta_s & |\beta|^2 \sin^2 2\theta_s \end{bmatrix} \tag{22}$$

and the generalised double-bounce model is given by

$$\mathbf{T}_d(\theta_d) = \mathbf{R}\mathbf{T}_d\mathbf{R}^T = \begin{bmatrix} |\alpha|^2 & \alpha \cos 2\theta_d & -\alpha \sin 2\theta_d \\ \alpha^* \cos 2\theta_d & \cos^2 2\theta_d & -\frac{1}{2}\sin 4\theta_d \\ -\alpha^* \sin 2\theta_d & -\frac{1}{2}\sin 4\theta_d & \sin^2 2\theta_d \end{bmatrix}, \tag{23}$$

where $|\alpha|$ and $|\beta| < 1$. The rotation matrix $\mathbf{R}$ is defined as

$$\mathbf{R} = \begin{bmatrix} 1 & 0 & 0 \\ 0 & \cos 2\theta & \sin 2\theta \\ 0 & -\sin 2\theta & \cos 2\theta \end{bmatrix}. \tag{24}$$

By setting β to zero, $\mathbf{T}_s(\theta_s)$ becomes

$$\dot{\mathbf{T}}_s = \begin{bmatrix} 1 & 0 & 0 \\ 0 & 0 & 0 \\ 0 & 0 & 0 \end{bmatrix} \tag{25}$$

which is roll-invariant, i.e., $\dot{\mathbf{T}}_s = \mathbf{R}\dot{\mathbf{T}}_s\mathbf{R}^T$. Note that (25) is also the coherency matrix for a spherical or trihedral radar target. If $\alpha = 0$, then $\mathbf{T}_d(\theta_d)$ reduces to a symmetric matrix:

$$\dot{\mathbf{T}}_d(\theta_d) = \begin{bmatrix} 0 & 0 & 0 \\ 0 & \cos^2 2\theta_d & -\frac{1}{2}\sin 4\theta_d \\ 0 & -\frac{1}{2}\sin 4\theta_d & \sin^2 2\theta_d \end{bmatrix}. \tag{26}$$

Furthermore, $\dot{\mathbf{T}}_d(\theta_d)$ turns into the following form if $\theta_d = 0$:

$$\dot{\mathbf{T}}_d = \begin{bmatrix} 0 & 0 & 0 \\ 0 & 1 & 0 \\ 0 & 0 & 0 \end{bmatrix}. \tag{27}$$

As inspired by the generalised odd-bounce and double-bounce scattering models, two modified four-component decompositions are introduced in Lee *et al*. (2018):

$$\mathbf{T} = f_s\mathbf{T}_s(\theta_s) + f_d\mathbf{T}_d + f_v\mathbf{T}_v + f_h\mathbf{T}_h \tag{28}$$

and

$$\mathbf{T} = f_s\mathbf{T}_s + f_d\mathbf{T}_d(\theta_d) + f_v\mathbf{T}_v + f_h\mathbf{T}_h. \tag{29}$$

If $\theta_s = 0$ in (28) or $\theta_d = 0$ in (29), then it means no rotation about the radar line of sight. Hence, (28) or (29) becomes the four-component decomposition derived by Yamaguchi *et al*. (2006), which is discussed in Section 2. Their solutions for f_s, f_d, and f_v can be adopted in this case.

From (28), there are nine equations with nine unknowns: (11), (16),

$$t_{22} = f_s |\beta|^2 \cos^2 2\theta_s + f_d + f_v/4 + f_h/2, \tag{30}$$
$$t_{33} = f_s |\beta|^2 \sin^2 2\theta_s + f_v/4 + f_h/2, \tag{31}$$
$$\Re(t_{12}) = f_s\Re(\beta^*) \cos 2\theta_s + f_d\Re(\alpha), \tag{32}$$
$$\Im(t_{12}) = f_s\Im(\beta^*) \cos 2\theta_s + f_d\Im(\alpha), \tag{33}$$
$$\Re(t_{13}) = -f_s\Re(\beta^*) \sin 2\theta_s, \tag{34}$$
$$\Im(t_{13}) = -f_s\Im(\beta^*) \sin 2\theta_s, \tag{35}$$
$$\Re(t_{23}) = -f_s |\beta|^2 \cos 2\theta_s \sin 2\theta_s. \tag{36}$$

After some algebraic manipulations, the rotation angle θ_s can be obtained by solving

$$a_1 \tan^3(2\theta_s) + a_2 \tan^2(2\theta_s) + a_3 \tan(2\theta_s) + a_4 = 0 \tag{37}$$

with

$$\begin{aligned}
a_1 &= 2\,[\Re(t_{23})]^2, \\
a_2 &= 4\,c_{33}\,\Re(t_{23}) - t_{11}\,\Re(t_{23}) - 2\,c_{22}\,\Re(t_{23}), \\
a_3 &= t_{11}c_{22} - t_{11}c_{33} - 2\,c_{22}c_{33} + 2\,[c_{33}]^2 - 2\,[\Re(t_{23})]^2 - [\Re(t_{12})]^2 - [\Im(t_{12})]^2 - [\Re(t_{13})]^2 - [\Im(t_{13})]^2, \\
a_4 &= t_{11}\Re(t_{23}) - 2\,c_{33}\Re(t_{23}) - 2\,\Re(t_{12})\,\Re(t_{13}) - 2\,\Im(t_{12})\,\Im(t_{13}) \\
&\quad + (c_{22} - c_{33})\,([\Re(t_{13})]^2 + [\Im(t_{13})]^2) / \Re(t_{23}),
\end{aligned} \tag{38}$$

where $c_{22} = t_{22} - f_h/2$ and $c_{33} = t_{33} - f_h/2$. The value of f_h is given by

$$f_h = 2\,|\Im(t_{23})|. \tag{39}$$

In (37), it is obvious that $\tan(2\theta_s)$ takes three roots of a cubic equation. For non-zero real values of θ_s, the solution of f_s is given by

$$f_s = -\left([\Re(t_{13})]^2 + [\Im(t_{13})]^2 \right) / \left[\Re(t_{23}) \tan(2\theta_s) \right]. \tag{40}$$

The remaining six unknowns can then be solved by substituting f_h, f_s, and θ_s into (30) to (36).

From (29), we also have nine equations with nine unknowns: (11), (16),

$$t_{22} = f_s |\beta|^2 + f_d \cos^2 2\theta_d + f_v/4 + f_h/2, \tag{41}$$
$$t_{33} = f_d \sin^2 2\theta_d + f_v/4 + f_h/2, \tag{42}$$
$$\Re(t_{12}) = f_s\Re(\beta^*) + f_d\Re(\alpha) \cos 2\theta_d, \tag{43}$$
$$\Im(t_{12}) = f_s\Im(\beta^*) + f_d\Im(\alpha) \cos 2\theta_d, \tag{44}$$
$$\Re(t_{13}) = -f_d\Re(\alpha) \sin 2\theta_d, \tag{45}$$
$$\Im(t_{13}) = -f_d\Im(\alpha) \sin 2\theta_d, \tag{46}$$
$$\Re(t_{23}) = -f_d \cos 2\theta_d \sin 2\theta_d. \tag{47}$$

Similarly, the rotation angle θ_d can be solved through

$$a_1 \tan^3(2\theta_d) + a_2 \tan^2(2\theta_d) + a_3 \tan(2\theta_d) + a_4 = 0, \tag{48}$$

where a_1, a_2, a_3, and a_4 are given separately in (38). In the cases with non-zero real values of θ_d, the value of f_h is computed based on (39) and the remaining seven unknowns can be successively obtained from (41) to (47). By taking out the helix scattering, (28) and (29) become three-component decompositions with only eight equations and eight unknowns. The solutions follow the same manner, where f_h is equal to zero.

One might be interested in setting $\theta_s = \theta_d = \theta$, which yields

$$\mathbf{T} = f_s\mathbf{T}_s(\theta) + f_d\mathbf{T}_d(\theta) + f_v\mathbf{T}_v + f_h\mathbf{T}_h. \tag{49}$$

From (49), we have (11), (16),

$$t_{22} = f_s |\beta|^2 \cos^2 2\theta + f_d \cos^2 2\theta + f_v/4 + f_h/2, \tag{50}$$
$$t_{33} = f_s |\beta|^2 \sin^2 2\theta + f_d \sin^2 2\theta + f_v/4 + f_h/2, \tag{51}$$
$$\Re(t_{12}) = f_s\Re(\beta^*) \cos 2\theta + f_d\Re(\alpha) \cos 2\theta, \tag{52}$$
$$\Im(t_{12}) = f_s\Im(\beta^*) \cos 2\theta + f_d\Im(\alpha) \cos 2\theta, \tag{53}$$
$$\Re(t_{13}) = -f_s\Re(\beta^*) \sin 2\theta - f_d\Re(\alpha) \sin 2\theta, \tag{54}$$

$$\Im(t_{13}) = -f_s\Im(\beta^*)\sin 2\theta - f_d\Im(\alpha)\sin 2\theta, \quad (55)$$

$$\Re(t_{23}) = -f_s|\beta|^2\cos 2\theta \sin 2\theta - f_d\cos 2\theta \sin 2\theta. \quad (56)$$

It can be easily observed that (52)–(55) are actually dependent equations, i.e.,

$$\Re(t_{13}) / \Re(t_{12}) = \Im(t_{13}) / \Im(t_{12}). \quad (57)$$

Consequently, there exist less than nine independent equations and (49) is thus not taken into consideration.

By letting $\alpha = \beta = 0$, (28) becomes

$$\mathbf{T} = f_s\dot{\mathbf{T}}_s + f_d\dot{\mathbf{T}}_d + f_v\mathbf{T}_v + f_h\mathbf{T}_h \quad (58)$$

and (29) turns into

$$\mathbf{T} = f_s\dot{\mathbf{T}}_s + f_d\dot{\mathbf{T}}_d(\theta_d) + f_v\mathbf{T}_v + f_h\mathbf{T}_h. \quad (59)$$

From (58), there are four equations with four unknowns: (13), (16),

$$t_{11} = f_s + f_v/2, \quad (60)$$

$$t_{22} = f_d + f_v/4 + f_h/2. \quad (61)$$

The solutions for f_s, f_d, f_v, and f_h are straightforward. From (59), we have five equations with five unknowns: (16), (42), (47), (60),

$$t_{22} = f_d\cos^2 2\theta_d + f_v/4 + f_h/2. \quad (62)$$

The rotation angle θ_d can be computed from

$$\Re(t_{23})\tan^2(2\theta_d) - (t_{22} - t_{33})\tan(2\theta_d) - \Re(t_{23}) = 0. \quad (63)$$

In fact, (63) can also be written as

$$-4\theta_d = \tan^{-1}[\,2\,\Re(t_{23}) / (t_{22} - t_{33})\,]. \quad (64)$$

It is interesting to note that (64) is related to the polarisation orientation angle in Lee and Ainsworth (2011, p. 55) and the rotation angle in Yamaguchi *et al*. (2011, p. 2254). The existence of negative sign in (64) is due to the anticlockwise definition of θ_d. For the three-component decomposition without helix scattering, (58) reduces to three equations with three unknowns, while (59) possesses only four equations with four unknowns.

From (13), (30), (31), (39), (41), (42), (61), and (62), it can be easily noticed that all the four-component decompositions require $t_{22} > |\Im(t_{23})|$ and $t_{33} > |\Im(t_{23})|$. If these requirements are unfulfilled, then all the decompositions are mathematically invalid. A negative value of f_v occurs, for examples, if f_s in (31) and f_d in (42) and (62) is positive.

The multistage four-component polarimetric decomposition consists of three processing stages. In the first stage (i.e., $\theta_s = \theta_d = 0$), the Yamaguchi's four-component decomposition is employed to obtain f_s, f_d, and f_v. Those pixels with negative value of f_s, f_d or f_v are marked as negative power pixels. Meanwhile, those pixels with all positive f_s, f_d, and f_v, but $|\alpha|$ or $|\beta| \geq 1$, are marked as incorrect positive power pixels.

In the second stage, the decompositions are applied to those marked pixels based on (28) and (29). As aforementioned, a set of f_s, f_d, and f_v values can be derived for each non-zero real rotation angle (θ_s or θ_d). Only the set, which fulfils the following criteria, is selected: (i) f_s, f_d, and $f_v > 0$, (ii) $|\alpha|^2$ and $|\beta|^2 < 1$, (iii) $|\alpha|^2 < \cos^2 2\theta_d$. Note that the third criterion is required merely for (29).

In the third stage (i.e., $\alpha = \beta = 0$), the decompositions are performed based on (58) and (59) for the remaining marked pixels from the second stage, where the set with all positive f_s, f_d, and f_v is selected. It is important to note here that the quadratic equation in (63) is used for calculating the rotation angle θ_d in (59).

4. ALOS-2 PALSAR-2 DATA

Covering a large area of Penang and Kerian District of Perak in Peninsular Malaysia, the ALOS-2 PALSAR-2 single-look complex data (level 1.1) were provided by Japan Aerospace Exploration Agency (JAXA). The test data (scene ID: ALOS2096050090-160303) were acquired on 3rd of March 2016 (17:30 UTC) containing four SAR image files, one leader file, one volume directory file, and one trailer file. The numbers of range and azimuth pixels in the SAR image file were 8512 and 25961, respectively. From the data set summary record in the leader file, the range pixel spacing was found to be 2.8608445 m, while the azimuth pixel spacing was 2.7986920 m.

In the ALOS-2 PALSAR-2 single-look slant-range quad-polarisation data, each pixel can be represented by a three-dimensional complex vector after symmetrising the cross-polarised responses:

$$\mathbf{s} = \begin{bmatrix} s_{\mathrm{HH}} \\ \sqrt{2}s_{\mathrm{HV}} \\ s_{\mathrm{VV}} \end{bmatrix} = c \begin{bmatrix} I_{\mathrm{HH}} + jQ_{\mathrm{HH}} \\ \{(I_{\mathrm{HV}} + I_{\mathrm{VH}}) + j(Q_{\mathrm{HV}} + Q_{\mathrm{VH}})\}/\sqrt{2} \\ I_{\mathrm{VV}} + jQ_{\mathrm{VV}} \end{bmatrix}. \tag{65}$$

The 32-bit in-phase and quadrature components are denoted separately by I and Q. The scalar c equals to $10^{(\mathrm{CF}-32)/20}$, where the value of the calibration factor (CF) is −83 (Motohka *et al*., 2018). In this study a four-look polarimetric covariance matrix was formed by taking 2×2 neighbouring pixels. After the multilooking, the image size was reduced to 4256 columns and 12980 rows.

5. EXPERIMENTAL RESULTS

The boxcar filter with a 3×3 window was first applied to the multilook ALOS-2 PALSAR-2 data. The coherency matrix was then obtained through a linear conversion from the filtered covariance matrix (Cloude and Pottier, 1996, p. 501). Afterwards, the ALOS-2 PALSAR-2 filtered data were used as the inputs for the polarimetric decomposition.

5.1 Negative Power Problem

As mentioned in Section 1, one well-known problem associated with the model-based decomposition is the presence of negative scattering powers. Figure 1(b) and Figure 1(c) show separately the distribution of the negative power and incorrect positive power pixels over a selected area of Penang Hill resulting from both the Yamaguchi's and multistage four-component decompositions. By comparing with Figure 1(b), the negative power pixels were lesser over Teluk Bahang Dam in Figure 1(c). Meanwhile, more negative power pixels over the Penang Hill were removed. The number of the negative power pixels in the entire Yamaguchi's decomposition output was about 31.2%. The amount reduced to around 4.8% by using the multistage four-component decomposition. Table 1 tabulates the exact numbers of the negative power and incorrect positive power pixels for both the Yamaguchi's and multistage four-component decompositions.

Table 1: Number of negative power and incorrect positive power pixels

	Negative power pixels	Incorrect positive power pixels
Volume scattering model based on uniform distribution		
Yamaguchi's four-component decomposition	17245340	390485
Multistage four-component decomposition	2638494	-
Volume scattering model with total randomness		
Yamaguchi's four-component decomposition	11808286	38822
Multistage four-component decomposition	465010	-

For comparison, another volume scattering model with total randomness, which was proposed by An *et al*. (2010, p. 2734), was employed. Its coherency matrix has the form

$$\mathbf{T}_{\mathrm{v}} = \frac{1}{3}\begin{bmatrix} 1 & 0 & 0 \\ 0 & 1 & 0 \\ 0 & 0 & 1 \end{bmatrix}. \tag{66}$$

This roll-invariant volume scattering model is also obtainable from (1) in Freeman (2007, p. 2584) by setting $\rho = 0$. The resultant numbers of the negative power and incorrect positive power pixels are listed in Table 1, where the numbers are apparently lower than those based on uniform distribution. Figure 1(d) shows a significant reduction of the negative power pixels over the Penang Hill after applying the multistage four-component decomposition. Similar to our previous findings in Lee *et al*. (2018), some of the remaining negative power pixels belonged to man-made objects, such as buildings, bridges, floating aquaculture farms etc. These negative power pixels exhibited $t_{22} < |\,\Im(t_{23})\,|$ or $t_{33} < |\,\Im(t_{23})\,|$, which caused the multistage four-component decomposition to be invalid. Moreover, many sea pixels were also found in this study to have such identical characteristics. Table 2 provides the exact number of the invalid pixels found in the entire ALOS-2 PALSAR-2 filtered data.

By considering and combining both the three-component and four-component decompositions together, an iterative multistage polarimetric decomposition was established, where its design is given in Figure 2. The iterative multistage decomposition was first performed by using the volume scattering model based on uniform distribution, followed by the volume scattering model with total randomness. From the obtained result, the total number of the negative power pixels was further reduced to less than 0.08%, i.e., 41673 pixels.

Table 2: Number of invalid pixels

$t_{22} < \lvert \Im(t_{23}) \rvert$	$t_{33} < \lvert \Im(t_{23}) \rvert$	$t_{22} < \lvert \Im(t_{23}) \rvert$ and $t_{33} < \lvert \Im(t_{23}) \rvert$
9688	384408	-

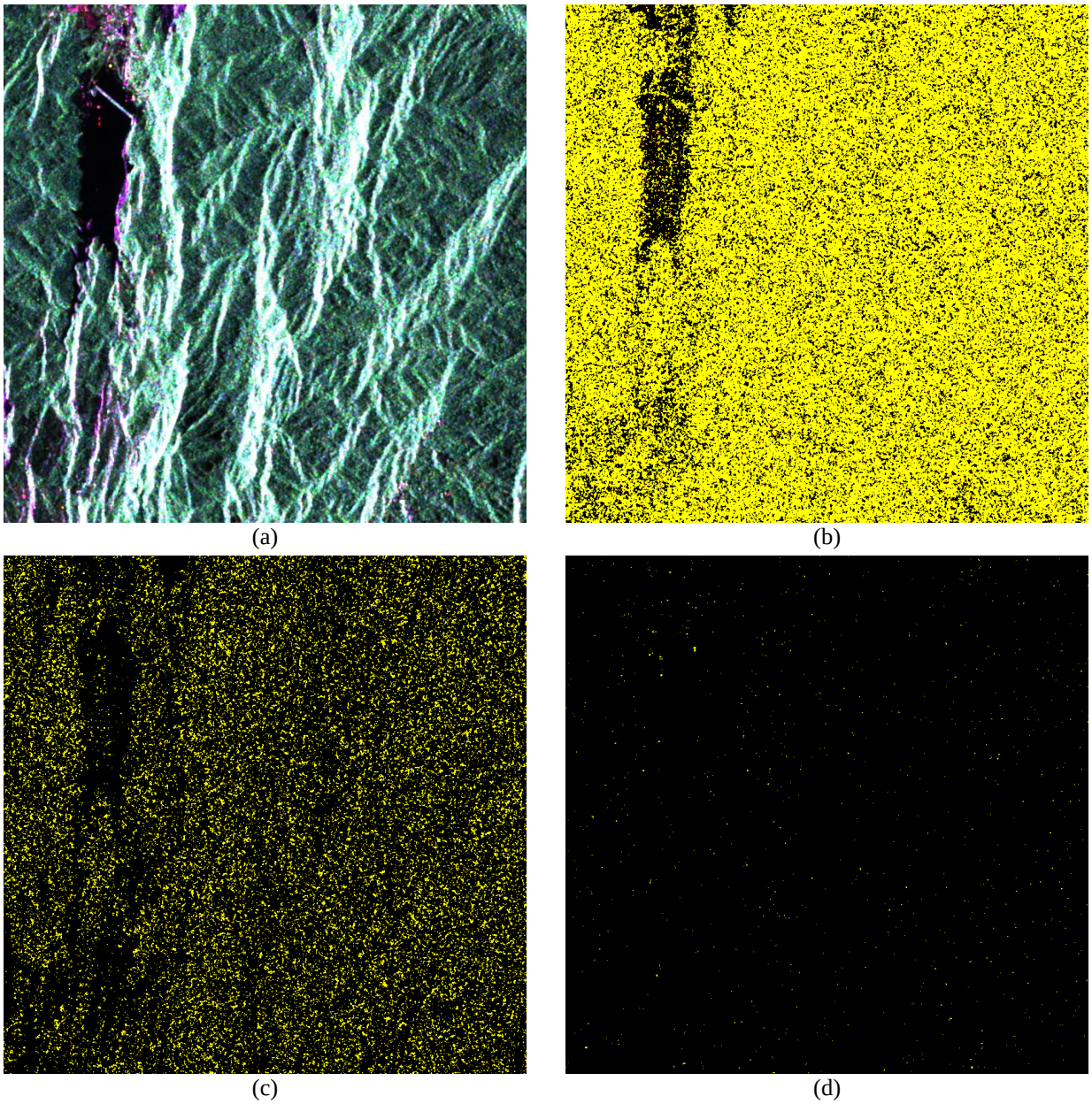

(a) (b) (c) (d)

Figure 1: The distribution of negative power pixels and incorrect positive power pixels. (a) A subset of the ALOS-2 PALSAR-2 data over Penang Hill, where Teluk Bahang Dam is located near the top-left corner. The HH, HV, and VV intensities are displayed in the red, green, and blue (RGB) colour space. (b) and (c) show separately the Yamaguchi's and multistage four-component decompositions with volume scattering model based on uniform distribution. (d) Multistage four-component decomposition by using volume scattering model with total randomness. In (b)–(d), the negative power pixels and the incorrect positive power pixels are coloured in yellow and red, respectively.

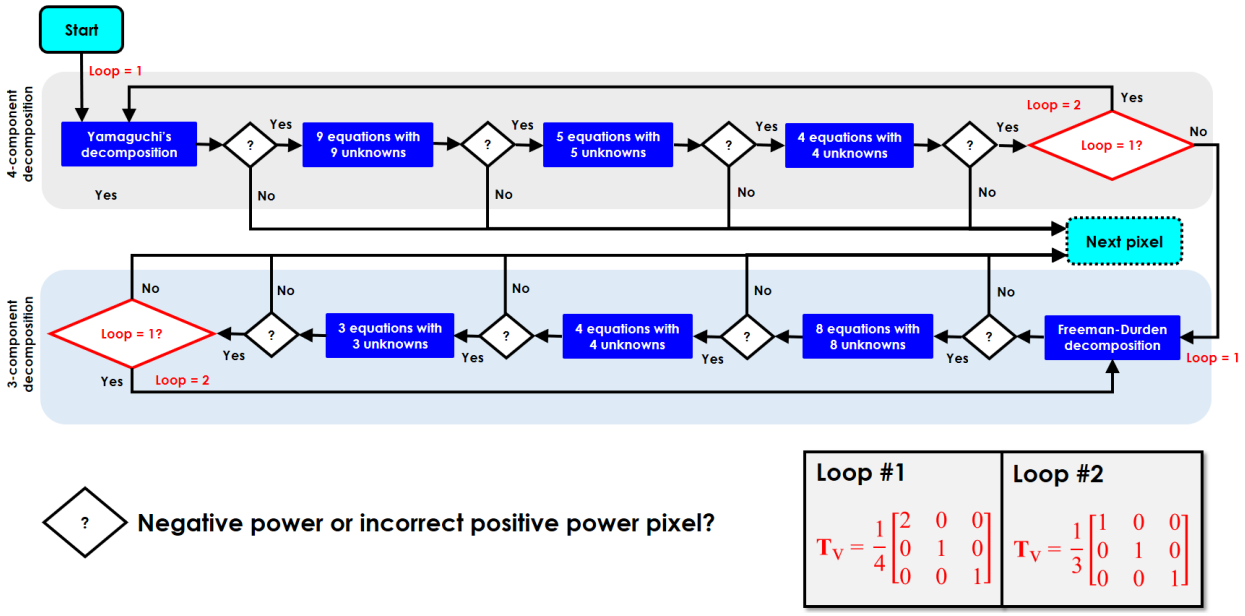

Figure 2: Iterative multistage polarimetric decomposition, which operates on a pixel-by-pixel basis

5.2 Scattering Classification

For the scattering classification, each pixel is categorised by comparing its decomposed powers and identifying the dominant scattering contribution. For example, a pixel belongs to volume scattering if $P_v > P_s$, $P_v > P_d$, and $P_v > P_h$. Figure 3 presents a subset of the dominant scattering classification output over rice paddy fields in Kerian District resulting from the iterative multistage polarimetric decomposition. A small fishing village called Tanjung Piandang is situated near the top-left corner in Figure 3(a).

The percentage of different scattering mechanisms of selected land cover classes is given in Table 3. The bare land, cleared land, and rice paddy field showed predominantly the surface scattering, i.e., more than 98%. Both the dryland forest and shrub were largely dominated by the volume scattering. The mangrove forest was characterised as having the dominant volume scattering (82.65%), followed by the surface scattering (15.16%). For the oil palm plantation estates, both the surface scattering (51.68%) and volume scattering (45.66%) were mostly detected. The double-bounce scattering was the main scattering component of the Penang Bridge, which contributed more than 85%. The Penang Port manifested its dominant double-bounce scattering of about 79.06%. The double-bounce scattering mechanism was expectably generated by the radar wave interactions between the cargo containers and the ground. In the first built-up area (i.e., built-up 1), the buildings were almost perpendicular to the radar illumination. The double-bounce scattering was dominant as a result of the successive reflections from the wall-ground structures. In contrast, the second built-up area (i.e., built-up 2) comprised the oriented buildings, which were not perpendicular to the radar illumination. These buildings showed a mixture of the surface, double-bounce, volume, and helix scattering mechanisms. The surface, double-bounce, volume, and helix scattering contributions were 26.48%, 14.93%, 58.35%, and 0.24%, respectively.

6. CONCLUSIONS

Applying on the ALOS-2 PALSAR-2 fully polarimetric data, our previously proposed multistage four-component decomposition was first re-examined for reducing the negative power pixels. From the multistage four-component decomposition results, the negative power pixels over vegetated areas, such as dryland forest, mangrove forest, oil palm, and shrub, were reduced significantly. The remaining negative power pixels distributed notably over man-made objects and sea. By integrating both the three-component and four-component decompositions, an iterative multistage decomposition was subsequently developed, which made use of two roll-invariant volume scattering models. The iterative multistage decomposition further reduced the total number of the negative power pixels to less than 0.08%.

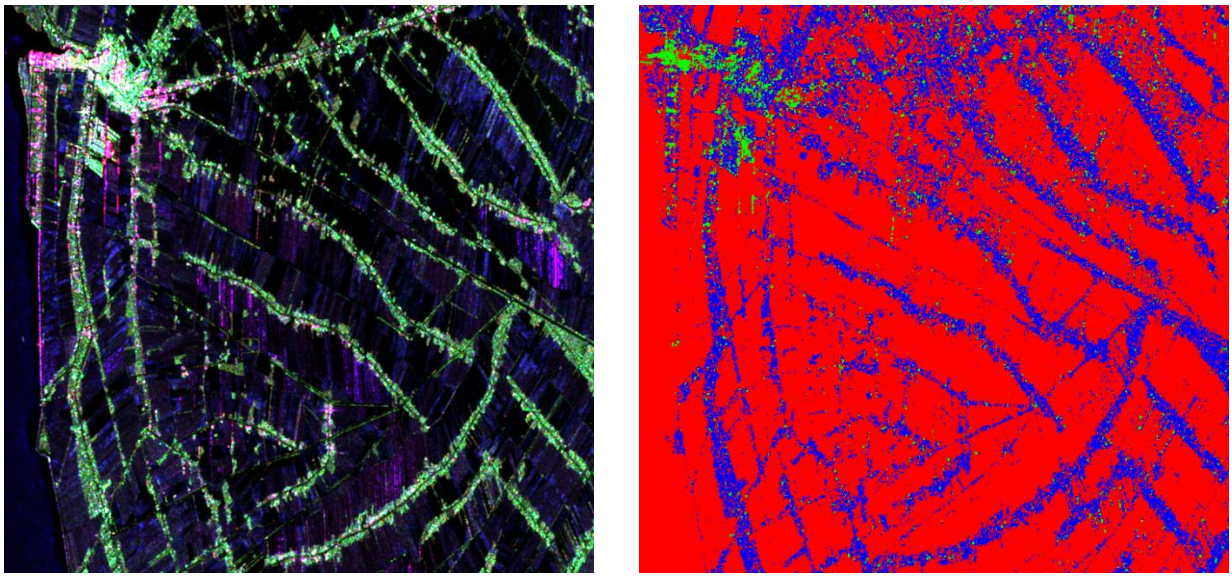

(a) (b)

Figure 3: (a) A subset of the ALOS-2 PALSAR-2 test data over rice paddy fields in Kerian District, where a small fishing village called Tanjung Piandang can be seen near the top-left corner. The HH, HV, and VV intensities are displayed in the RGB colour space. (b) The dominant scattering classification result of (a), where the surface, double-bounce, and volume scattering classes are coloured in red, green, and blue, respectively.

Table 3: Scattering mechanisms (in percent) of different land cover types

	Number of pixels	Surface	Double-bounce	Volume	Helix
Bare land	5087	**98.25**	0.63	1.12	-
Bridge	712	9.41	**85.95**	4.64	-
Built-up 1	10223	24.75	**73.70**	1.55	-
Built-up 2	23804	26.48	14.93	58.35	0.24
Cleared land	10359	**99.96**	-	0.04	-
Dryland forest	126615	5.80	0.43	**93.71**	0.06
Mangrove forest	88564	15.16	2.17	**82.65**	0.02
Oil palm	22416	51.68	2.66	45.66	-
Port	1853	15.87	**79.06**	4.96	0.11
Rice paddy field	31778	**99.26**	0.04	0.70	-
Shrub	3580	8.02	0.44	**91.54**	-

ACKNOWLEDGEMENT

The authors would like to express their gratitude to JAXA for providing the ALOS-2 PALSAR-2 data under the 2nd Earth Observation Research Announcement Collaborative Research Agreement.

REFERENCES

W. An, Y. Cui, and J. Yang (2010). Three-Component Model-Based Decomposition for Polarimetric SAR Data. *IEEE Transactions on Geoscience and Remote Sensing*, 48(6), pp. 2732–2739.

M. Arii, J. J. van Zyl, and Y. Kim (2011). Adaptive Model-Based Decomposition of Polarimetric SAR Covariance Matrices. *IEEE Transactions on Geoscience and Remote Sensing*, 49(3), pp. 1104–1113.

S.-W. Chen, X.-S. Wang, S.-P. Xiao, and M. Sato (2014). General Polarimetric Model-Based Decomposition for Coherency Matrix. *IEEE Transactions on Geoscience and Remote Sensing*, 52(3), pp. 1843–1855.

S. R. Cloude and E. Pottier (1996). A Review of Target Decomposition Theorems in Radar Polarimetry. *IEEE Transactions on Geoscience and Remote Sensing*, 34(2), pp. 498–518.

S. R. Cloude and E. Pottier (1997). An Entropy Based Classification Scheme for Land Applications of Polarimetric SAR. *IEEE Transactions on Geoscience and Remote Sensing*, 35(1), pp. 68–78.

A. Freeman (2007). Fitting a Two-Component Scattering Model to Polarimetric SAR Data from Forests. *IEEE Transactions on Geoscience and Remote Sensing*, 45(8), pp. 2583–2592.

A. Freeman and S. Durden (1992). A Three-Component Scattering Model to Describe Polarimetric SAR Data. *SPIE Proceedings*, vol. 1748, pp. 213–224.

A. Freeman and S. L. Durden (1998). A Three-Component Scattering Model for Polarimetric SAR Data. *IEEE Transactions on Geoscience and Remote Sensing*, 36(3), pp. 963–973.

S.-H. Hong and S. Wdowinski (2014). Double-Bounce Component in Cross-Polarimetric SAR from a New Scattering Target Decomposition. *IEEE Transactions on Geoscience and Remote Sensing*, 52(6), pp. 3039–3051.

J.-S. Lee and T. L. Ainsworth (2011). The Effect of Orientation Angle Compensation on Coherency Matrix and Polarimetric Target Decompositions. *IEEE Transactions on Geoscience and Remote Sensing*, 49(1), pp. 53–64.

J.-S. Lee, T. L. Ainsworth, and Y. Wang (2014). Generalized Polarimetric Model-Based Decompositions Using Incoherent Scattering Models. *IEEE Transactions on Geoscience and Remote Sensing*, 52(5), pp. 2474–2491.

K. Y. Lee, C. G. Hou, J. X. Chen, S. C. Liew, and L. K. Kwoh (2018). Model-Based Decomposition with Reduced Negative Scattering Powers. *Proceedings of the IEEE International Geoscience and Remote Sensing Symposium*, pp. 4547–4550.

T. Motohka, O. Isoguchi, M. Sakashita, and M. Shimada (2018). Results of ALOS-2 PALSAR-2 Calibration and Validation After 3 Years of Operation. *Proceedings of the IEEE International Geoscience and Remote Sensing Symposium*, pp. 4169–4170.

G. Singh and Y. Yamaguchi (2018). Model-Based Six-Component Scattering Matrix Power Decomposition. *IEEE Transactions on Geoscience and Remote Sensing*, 56(10), pp. 5687–5704.

J. J. van Zyl (1989). Unsupervised Classification of Scattering Behavior Using Radar Polarimetry Data. *IEEE Transactions on Geoscience and Remote Sensing*, 27(1), pp. 36–45.

J. J. van Zyl, M. Arii, and Y. Kim (2011). Model-Based Decomposition of Polarimetric SAR Covariance Matrices Constrained for Nonnegative Eigenvalues. *IEEE Transactions on Geoscience and Remote Sensing*, 49(9), pp. 3452–3459.

J. J. van Zyl, Y. Kim, and M. Arii (2008). Requirements for Model-Based Polarimetric Decompositions. *Proceedings of the IEEE International Geoscience and Remote Sensing Symposium*, pp. V-417–V-420.

Y. Yajima, Y. Yamaguchi, R. Sato, H. Yamada, and W.-M. Boerner (2008). PolSAR Image Analysis of Wetlands Using a Modified Four-Component Scattering Power Decomposition. *IEEE Transactions on Geoscience and Remote Sensing*, 46(6), pp. 1667–1673.

Y. Yamaguchi, T. Moriyama, M. Ishido, and H. Yamada (2005). Four-Component Scattering Model for Polarimetric SAR Image Decomposition. *IEEE Transactions on Geoscience and Remote Sensing*, 43(8), pp. 1699–1706.

Y. Yamaguchi, A. Sato, W.-M. Boerner, R. Sato, and H. Yamada (2011). Four-Component Scattering Power Decomposition With Rotation of Coherency Matrix. *IEEE Transactions on Geoscience and Remote Sensing*, 49(6), pp. 2251–2258.

Y. Yamaguchi, Y. Yajima, and H. Yamada (2006). A Four-Component Decomposition of PolSAR Images Based on the Coherency Matrix. *IEEE Geoscience and Remote Sensing Letters*, 3(3), pp. 292–296.